Nano Energy 79 (2021) 105386

Contents lists available at ScienceDirect

Nano Energy

journal homepage: http://www.elsevier.com/locate/nanoen

Full paper

Electron transfer in the contact-electrification between corrugated 2D materials: A first-principles study

Dan Tan [a,b], Morten Willatzen [a,b,*], Zhong Lin Wang [a,b,c]

[a] CAS Center for Excellence in Nanoscience, Beijing Key Laboratory of Micro-Nano Energy and Sensor, Beijing Institute of Nanoenergy and Nanosystems, Chinese Academy of Sciences, Beijing, 100083, China
[b] School of Nanoscience and Technology, University of Chinese Academy of Sciences, Beijing, 100049, China
[c] School of Materials Science and Engineering, Georgia Institute of Technology, Atlanta, GA, 30332, USA

ARTICLE INFO

Keywords:
Contact electrification
Flexoelectric effect
Electron transfer
First-principles theory

ABSTRACT

Triboelectricity usually occurs between two different materials and can be understood as electron transfer in the framework of the electron-cloud model. Recently, experiments have shown that charge transfer also can happen between chemically identical materials but different surface curvatures. To understand the driving mechanism for this case, we carry out, for the first time, first-principles density functional theory (DFT) investigations of charge transfer due to flexoelectricity and piezoelectricity in two-dimensional materials. Case studies of piezoelectric molybdenum telluride (2H–$MoTe_2$) and non-piezoelectric graphene are analyzed in detail. It is found that a large corrugation of the contacting materials, whether identical or not, causes a nonlinear increase in the charge transfer, leading to electron depletion near concave surfaces and electron accumulation near convex surfaces. The maximum charge transfer is found to occur around an equilibrium separation distance of the contacting materials. In the case of graphene, and different from 2H–$MoTe_2$, both piezoelectric and flexoelectric coefficients are found to increase as the corrugation increases and is followed by a bandgap opening. We stipulate that the present *ab initio* findings provide new insight toward understanding the origins of triboelectricity.

1. Introduction

In the past decade, triboelectric nanogenerators have received huge interest in science and technology [1–3]. When two materials are forced to contact, or rubbed against each other, charge transfer can happen whereby an electrostatic potential difference is established across the interfaces [4,5]. The electron-cloud model provides a simple picture to explain electron transfer as electron wavefunction overlap between states of coupled potential wells [6–8].

Experiments have shown that contact between two identical insulators produces static charges where convex and concave surfaces are prone to be negatively and positively charged, respectively [9,10]. Further, in some materials such as sand and grains, smaller and larger particles tend to be negatively and positively charged, respectively [11,12]. Flexoelectricity [13–16], the linear coupling between the electric polarization and strain gradient, has been proposed by Mizzi et al. [17] as the main reason that drives charge transfer. They demonstrated that the surface potential difference generated by flexoelectricity acts as a driver for triboelectric charge separation using approximative Hertzian and Johnson-Kendall-Roberts (JKR) models. Persson [18] developed these theories and studied the electric potential produced by flexoelectricity for elastic solids with a random surface roughness.

First-principles calculations have been carried out for quantitative studies. As for triboelectricity, Wu et al. [19,20] studied the contributions of different molecular groups in metal and amorphous polymers to contact electrification. They revealed that the contributions made by the same atomic species in different molecular groups are different. Li et al. [21] found that the hydrogen bonds of water molecules are the main electron donors at metal-polymer interfaces in a humid environment. As for flexoelectricity, Dreyer et al. [22] developed a first-principles method based on density-functional perturbation theory to obtain the clamped-ion flexoelectric tensors. Shi et al. [23] calculated flexoelectricity in wrinkled transition metal dichalcogenide monolayers and the contribution to the out-of-plane polarization. To our knowledge, no studies have hitherto investigated the combined influence of piezoelectricity and flexoelectricity for charge transfer which is essential to

* Corresponding author. CAS Center for Excellence in Nanoscience, Beijing Key Laboratory of Micro-Nano Energy and Sensor, Beijing Institute of Nanoenergy and Nanosystems, Chinese Academy of Sciences, Beijing, 100083, China.
E-mail address: mortenwillatzen@binn.cas.cn (M. Willatzen).

https://doi.org/10.1016/j.nanoen.2020.105386
Received 4 August 2020; Received in revised form 4 September 2020; Accepted 5 September 2020
Available online 18 September 2020

quantify their individual importance for triboelectricity.

In this work, we study two important two-dimensional (2D) materials and determine quantitatively the contributions of flexoelectricity and piezoelectricity to triboelectricity. The highly flexible feature makes 2D materials ideal for electromechanical applications especially due to the strongly scale-dependent flexoelectric effect. Here we choose a 2D transition metal dichalcogenide $MoTe_2$ (TMD) and graphene as representative piezoelectric and non-piezoelectric materials, respectively. Different from graphene, monolayer TMDs have three atoms along the out-of-plane direction, thus generating larger polarization when deformed. Among all the 2H-TMDs monolayers, $MoTe_2$ is found to have the largest piezoelectric coefficient e_{xxx} [24]. The influence of flexoelectricity and piezoelectricity for charge transfer in both 2H–$MoTe_2$ and graphene are studied using first-principles theory and we assess the importance of corrugation and separation distance for charge transfer.

2. Computational methods

All calculations are carried out using Density-Functional Theory (DFT) with the plane wave-based Vienna Ab initio Simulation Package (VASP) [25,26]. We use the projector-augmented wave method [27,28]. The generalized gradient approximation is employed for the exchange−correlation functional [29]. We use an energy cutoff for the plane wave of 550 eV and $2 \times 5 \times 1$ Gamma centered k-point meshes during geometry optimization and $4 \times 8 \times 1$ k-point meshes for the electronic properties calculations. The calculations are converged in energy to 10^{-6} eV/cell and the structures are allowed to relax until the forces are less than 2×10^{-2} eV/Å. A vacuum layer of 60 Å is inserted perpendicular to the 2D materials to avoid spurious interlayer interactions.

The Bader analysis is a well-established analysis tool for studying the topology of the charge density [30]. Within this formalism, each basin belonging to a particular atom is defined using a zero-flux surface in the charge density. The total charge assigned to this atom is obtained by integrating the charge density over the whole basin. Then, the atomic charge is equal to the difference between the nuclear charge and the total charge.

To figure out the reason behind charge transfer between two identical layers with corrugations, we study their polarization perpendicular to the surface. Born effective charge tensors are used in DFT-VASP [31] to calculate the dipole moment.

The dipole moment of each atom is calculated by

$$\partial \boldsymbol{d}_i = Z^*_{ij} \partial \boldsymbol{r}_j, \tag{1}$$

where Z^*_{ij} is the Born effective charge tensors and $\partial \boldsymbol{r}_j$ is the displacement. In our case, the displacement is defined corresponding to the flat configuration. Dipole moment along z direction is induced because of curvature, which can be calculated using Eq. (1), that is

$$\partial \boldsymbol{d}_3 = Z^*_{31} \partial \boldsymbol{r}_1 + Z^*_{32} \partial \boldsymbol{r}_2 + Z^*_{33} \partial \boldsymbol{r}_3. \tag{2}$$

Out-of-plane polarization along z direction is calculated using

$$P_3 = \frac{\sum_i \partial \boldsymbol{d}_3}{V}, \tag{3}$$

where V is the volume of all the involved atoms.

The charge density difference is calculated by $\Delta\rho = \rho_{\text{after}} - \rho_{\text{before}}$ [20,21], where ρ_{after} is the total charge density after contact, and ρ_{before} is the charge density before contact. ρ_{before} is calculated as $\rho_{\text{before}} = \rho_{\text{left}} + \rho_{\text{right}}$, where ρ_{left} and ρ_{right} are charge densities of the left and right layers, respectively.

3. Piezoelectric 2D materials

Firstly, we build a similar model containing 2D 2H–$MoTe_2$, shown in Fig. 1a. There are 16 Mo atoms (gray colored) and 32 Te atoms (pink colored). To maintain the corrugated structure during relaxation, Mo atoms are clamped and only the Te atoms are allowed to be fully relaxed. The model is divided into four parts to analyze the charge transfer for different corrugations and different separation distances. Evidently, Regions I and IV (II and III) are concave (convex) surfaces. Corrugation C, is defined as $C = A/\lambda$, where A and λ refer to the height and length of the wave, respectively.

3.1. Charge transfer between two identical layers with different corrugations

Different corrugations from 0% to 8% are chosen to study the effect of curvature on charge transfer at the same separation distance 7 Å, which is shown in Fig. 1b. Here the separation distance is defined as the distance between the same atoms in two layers. According to our calculations and symmetry, value of charge transfer between Regions I and III is the same as between Regions II and IV for two identical layers. Hence, in the following we use one number to represent the charge transfer between Regions I and III or, likewise, between Regions II and IV. Here we can see that charge transfer increases as the corrugation getting larger. A large corrugation leads to large polarization changes which act as a driving mechanism for contact electrification. For two flat identical materials, there is no charge transfer irrespective of the separation distance.

Since the two 2H–$MoTe_2$ layers are identical, we calculate the polarization along the z axis of the left layer in Fig. 1a. Fig. 2a shows the fitting curve of one 2H–$MoTe_2$ layer with corrugation of 3%. The associated calculated strain ε_{xz} and strain gradient $\frac{\partial \varepsilon_{xz}}{\partial x}$ curves are shown in Fig. 2b and c. The calculated polarization at the same positions along the z direction is represented by yellow circles in Fig. 2d, while the black curve is the fitting curve. Fig. 2e–h and Fig. 2i-l are for corrugations of 5% and 8%, respectively. The corresponding equations are shown in supplementary material, Table S1.

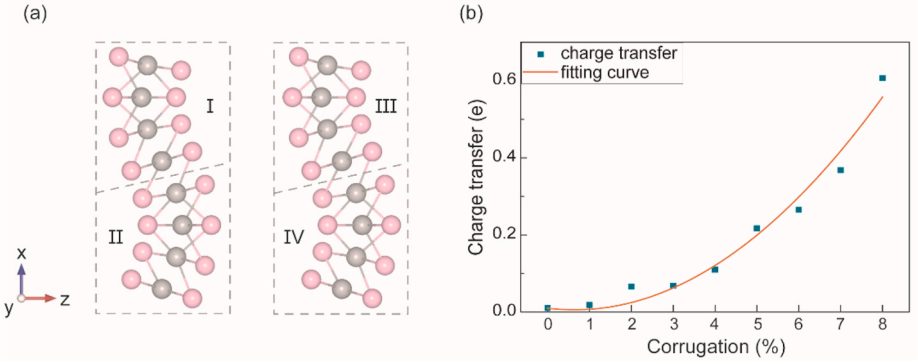

Fig. 1. (a) Diagram of the two curved 2H–$MoTe_2$ layers. (b) Charge transfer of different corrugations at a separation distance 7.0 Å.

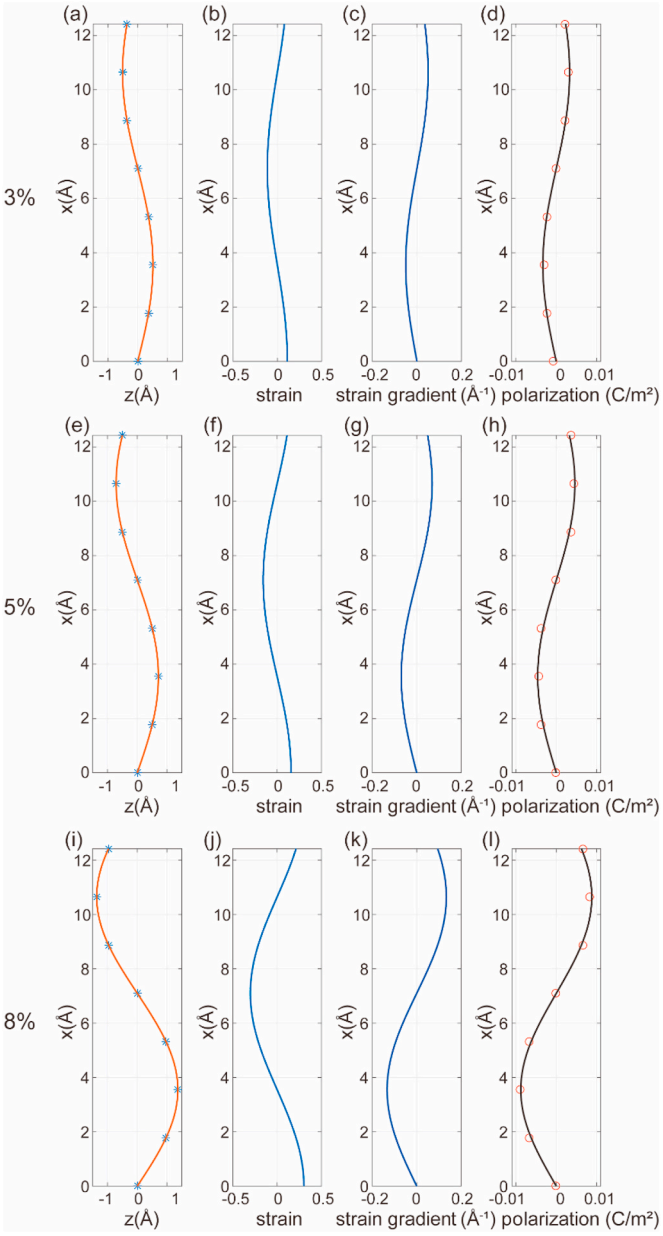

Fig. 2. Analysis of contribution to polarization $P_z(x)$ of 2H–$MoTe_2$ at different corrugations 3%, 5%, 8%. (a, e, i) Fitting curve. (b, f, j) Strain ε_{xz}. (c, g, k) Strain gradient $\frac{\partial \varepsilon_{xz}}{\partial x}$. (d, h, l) Fitting curve of the polarization component along the z axis.

From these analyses, we can see that the polarization along z axis are basically contributed from flexoelectric effect. The corresponding flexoelectric coefficient is

$$\mu_{zxzx} = \frac{P_z}{\frac{\partial \varepsilon_{xz}}{\partial x}} \approx 0.0066 \text{ nC/m}. \tag{4}$$

These calculations verify that large polarization changes originate from large corrugations. Thus we can conclude that the flexoelectric effect is the main reason that drives charge transfer and the piezoelectric coefficient e_{zxz} is negligible for all corrugations of $MoTe_2$.

3.2. Charge transfer between two identical layers with different separation distance

Fig. 3 shows the charge transfer of different separation distance where the corrugation is 8%. We choose a large distance of 15 Å to represent the situation that the two layers do not interact any longer, thus the charge redistribution is generated by corrugation only. In that view, all charge transfer results are determined by subtracting charge at large distance 15 Å to avoid local charging due to bonding effect. Besides, the total number of electrons stays the same at every separation distance. Here we can see that as the separation distance increases, the charge transfer increases at first, reaches its maximum value at a distance 7.0 Å, and for distances above decreases to zero.

The inset of Fig. 3 shows that the force between the two layers is repulsive (attractive) when the separation distance is smaller (larger) than 7 Å. A separation of 7 Å therefore corresponds to the equilibrium distance and smaller separations is only possible if an external force is applied to push the two layers closer. This qualitative dependence has been seen (Ref. [32]), where the absolute squared momentum overlap integral reaches a maximum value and then decreases to zero as the separation distance getting larger. Thus it can be concluded that the maximum charge transfer happens around the equilibrium separation in accordance with the overlapped electron-cloud theory [7,8].

3.3. Charge transfer between two layers with different shapes

In the above calculations, two identical 2H–$MoTe_2$ layers are placed with the same corrugation phase as shown in Fig. 4a. Since the charge transfers of different regions (shown in Fig. 1a) are the same, one number is sufficient to represent the charge transfer between regions. However, this ideal situation hardly exists in reality. To explore this further, we choose three models, shown in Fig. 4b–d, where b and c represent two layers with relative corrugation phases $\pi/2$ and π, respectively. Fig. 4d shows a model with one corrugated layer and one flat layer. All the four models correspond to the same corrugation level 8% and the same average separation distance 10 Å.

For each model we calculate the charge density difference to show the charge distribution. As shown in Fig. 4a–d, the yellow (blue) region shows regions of electron gain (loss). 2D projections of charge density differences are plotted to gain further insight into the charge distributions of the four different situation models, shown in Fig. 4e–h. Combining Fig. 4a and e, we can see that for two identically corrugated layers, electrons are depleted from concave surfaces and accumulated around convex surfaces, resulting in the former (latter) being positively (negatively) charged in good agreement with experimental results [9]. Fig. 4b and f shows the charge density difference of two 2H–$MoTe_2$ layers with a relative corrugation phase $\pi/2$. We can see that charge transfer mainly happens around the part where the separation distance is smallest, which is also seen in Fig. 4c and g when the two layers have a relative corrugation phase π. Fig. 4d and h shows the charge density difference of one corrugated layer and one flat layer. For the left corrugated layer, the convex surface is the main electron acceptor and the concave surface is the main electron donor, resulting in electron rearrangement around the flat layer, a situation which will not happen for two flat layers. In general, the charge density difference value of two identically corrugated layers is the smallest and the most uniformly distributed of all four model situations. For real interfaces, the local contacting models would be stochastically distributed in terms of corrugation.

4. Non-piezoelectric 2D materials

Similar models are built for graphene, which also has a honeycomb structure similar to the 2D transition metal-dichalcogenides in the 2H phase, but flat graphene is a non-piezoelectric material due to its centrosymmetry. As seen in Fig. 5a, there are 32C atoms in total. To maintain the corrugated structure, half of the carbon atoms are clamped along the z direction in an alternate manner.

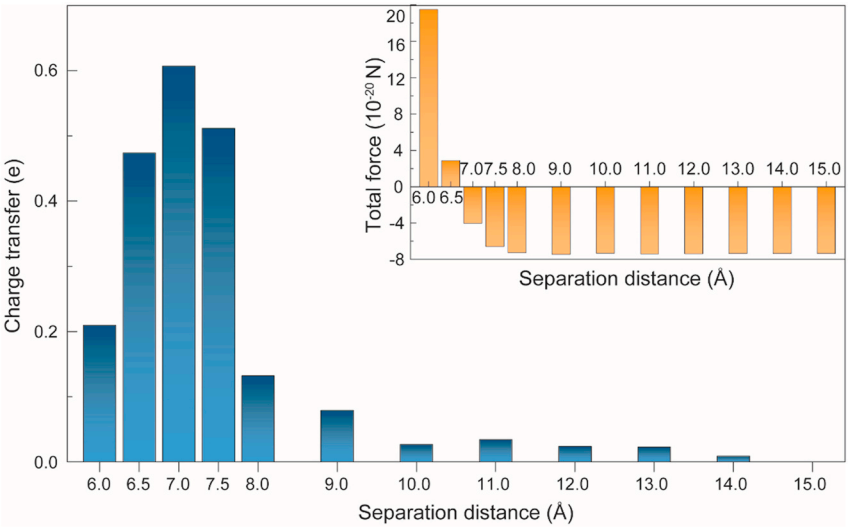

Fig. 3. Charge transfer of 2H–$MoTe_2$ at different separation distance where the corrugation is 8%. Inset: Corresponding force along z axis between two layers.

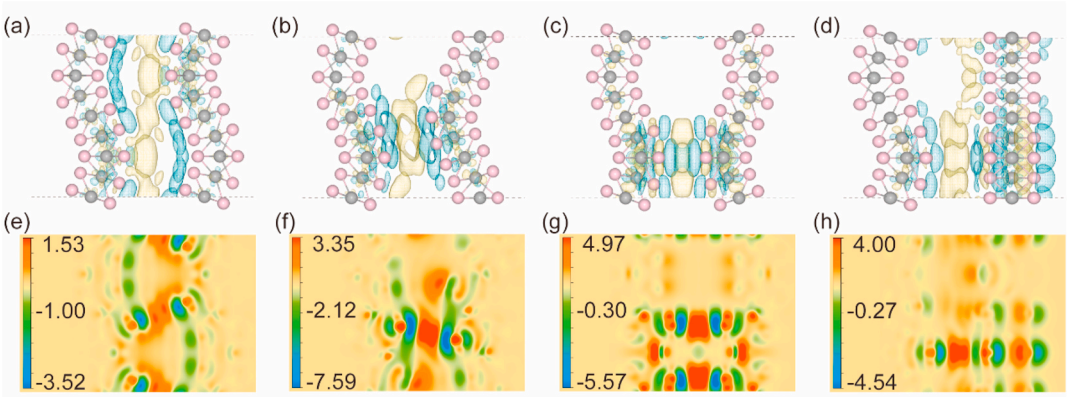

Fig. 4. Charge density differences of different 2H–$MoTe_2$ models: (a) two identical corrugated layers, (b) two layers with relative corrugation phase π/2, (c) two layers with relative corrugation phase π, (d) one corrugated layer and one flat layer (yellow region represents electron gain and blue region represents electron loss). (e–h) Corresponding 2D projections of charge density differences (in units of 10^{-4} e/Å^3).

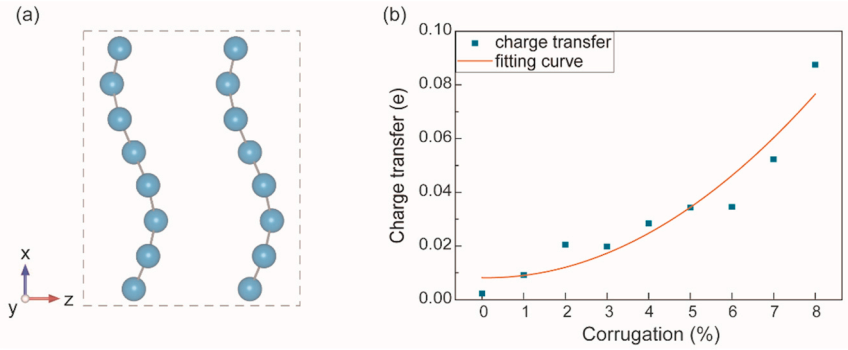

Fig. 5. (a) Diagram of the two curved graphene layers. (b) Charge transfer of different corrugations at a separation distance 3.0 Å.

4.1. Charge transfer between two identical layers with different corrugations

Charge transfer between two identical graphene layers are calculated at different corrugations from 0% to 8%, as shown in Fig. 5b, where the separation distance is 3.0 Å. As mentioned above and different from 2H–$MoTe_2$, corrugated graphene becomes piezoelectric while flat graphene (corrugation 0%) is non-piezoelectric. A large corrugation causes a nonlinear increase in the charge transfer similar to what we found for 2H–$MoTe_2$. Our results show, however, that the values of charge transfer between curved graphene layers are nearly 5 times smaller than those of 2H–$MoTe_2$ layers. We note that the electron affinity of graphene is 4.248 eV [33] while the electron affinity of 2H–$MoTe_2$ is 3.65 eV [34]. The lower the electron affinity is the lower the energy to remove an electron from the surface is, i.e., it is easier for electrons to escape a layer of 2H–$MoTe_2$ than graphene. Furthermore, the number of total electrons

of graphene is much smaller compared to 2H–$MoTe_2$ for the same dimensions.

Fig. 6a shows the fitting curve of the left graphene layer with corrugation of 3%. The calculated strain ε_{xz} and strain gradient $\frac{\partial \varepsilon_{xz}}{\partial x}$ curves are shown in Fig. 6b and c, respectively. The calculated polarization along the z direction is represented by red circles in Fig. 6d, while the black curve is the corresponding fitting curve. Fig. 6e–h and i-l correspond to corrugations of 5% and 8%, respectively. All the curve equations are shown in supplementary material, Table S2.

Unlike 2H–$MoTe_2$, both piezoelectricity and flexoelectricity contribute to the out-of-plane polarization of graphene, which can be expressed as $P_z(x) = e_{zxz}\varepsilon_{xz} + \mu_{zxzx}\frac{\partial \varepsilon_{xz}}{\partial x}$. Our calculated results reveal that the contribution from flexoelectricity is the main reason as it is approximately ten times larger than that from piezoelectricity. Another interesting observation is that both the piezoelectric coefficient e_{zxz} and the flexoelectric coefficient μ_{zxzx} depend on the corrugation, as Fig. 7a shows. They both increase as the corrugation increases. The flexoelectric coefficient μ_{zxzx} at a corrugation of 8% turns out to be larger than the one calculated for 2H–$MoTe_2$. Fig. 7b shows the Born effective charge Z^*_{33} of the top carbon atom in the left graphene layer, which also increases when the corrugation gets larger. Similar results were found in Ref. [35], namely that the piezoelectric coefficient and the Born effective charge attain giant values in gapped graphene independent of the symmetry-breaking mechanism (as soon as a finite bandgap opens). This phenomenon is not found in 2H–$MoTe_2$. The Born effective charges of 2H–$MoTe_2$ stay the same for different corrugations and the induced flexoelectric coefficient μ_{zxzx} is also a constant. As a semiconductor, monolayer 2H–$MoTe_2$ has a direct bandgap of ~1.1 eV which is nearly unchanged for different corrugations. Flat graphene has a zero bandgap. As its symmetry is broken, the bandgap is opened up from 0 eV to 0.5 eV and the polarization changes as well.

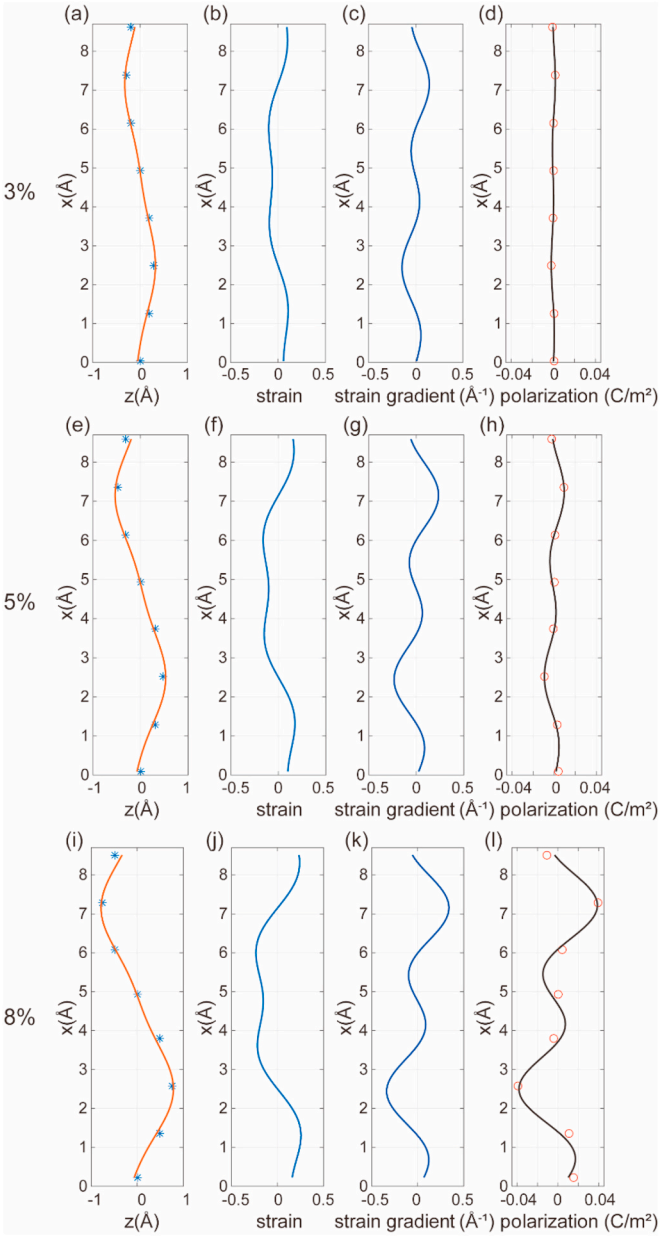

Fig. 6. Analysis of contribution to polarization $P_z(x)$ of graphene at different corrugations 3%, 5%, 8%. (a, e, i) Fitting curve. (b, f, j) Strain ε_{xz}. (c, g, k) Strain gradient $\frac{\partial \varepsilon_{xz}}{\partial x}$. (d, h, l) Fitting curve of polarization along z axis.

4.2. *Charge transfer between two identical layers with different separation distance*

Fig. 7c shows the charge transfer between two curved graphene layers at different separation distances for the case where the corrugation is 8%. We choose a large distance 10 Å to represent the situation that two layers do not interact, i.e., the charge redistribution is generated by the corrugation only. Here we can see that as the separation distance increases, the charge transfer increases at first, reaches the maximum value at distance 3 Å, and then decreases to zero. The Inset shows the corresponding force along the z axis between two layers. Its value is positive when the separation distance is smaller than 3 Å and changes to negative when it's larger than 3 Å. This finding suggests that the maximum charge transfer occurs around an equilibrium separation distance, a result which agrees with the above studied 2H–$MoTe_2$.

5. Conclusion

Triboelectric driving mechanisms between identical materials were studied using first-principles density functional theory calculations. We chose 2D piezoelectric material (2H–$MoTe_2$) and non-piezoelectric material (graphene) with different corrugations to determine quantitatively the contributions from flexoelectricity and piezoelectricity. It was demonstrated that flexoelectricity is the main driving mechanism for charge transfer. Unlike 2H–$MoTe_2$, both flexoelectric and piezoelectric coefficients of graphene increase as the corrugation increases. The change in symmetry of corrugated graphene vs. flat graphene makes the former piezoelectric and leads to the opening of a bandgap. Study of charge density differences showed that concave (convex) surfaces tend to be positively (negatively) charged which is in good agreement with experimental results. Our results also confirm that the maximum charge transfer occurs around an equilibrium separation distance.

Credit author contribution statement

Dan Tan: planned the idea of this research work. calculated all data and wrote the initial version of the paper, All results presented in the paper were discussed. **Morten Willatzen:** planned the idea of this research work. All results presented in the paper were discussed. **Zhong Lin Wang:** planned the idea of this research work. All results presented in the paper were discussed.

Declaration of competing interest

The authors declare that they have no known competing financial interests or personal relationships that could have appeared to influence the work reported in this paper.

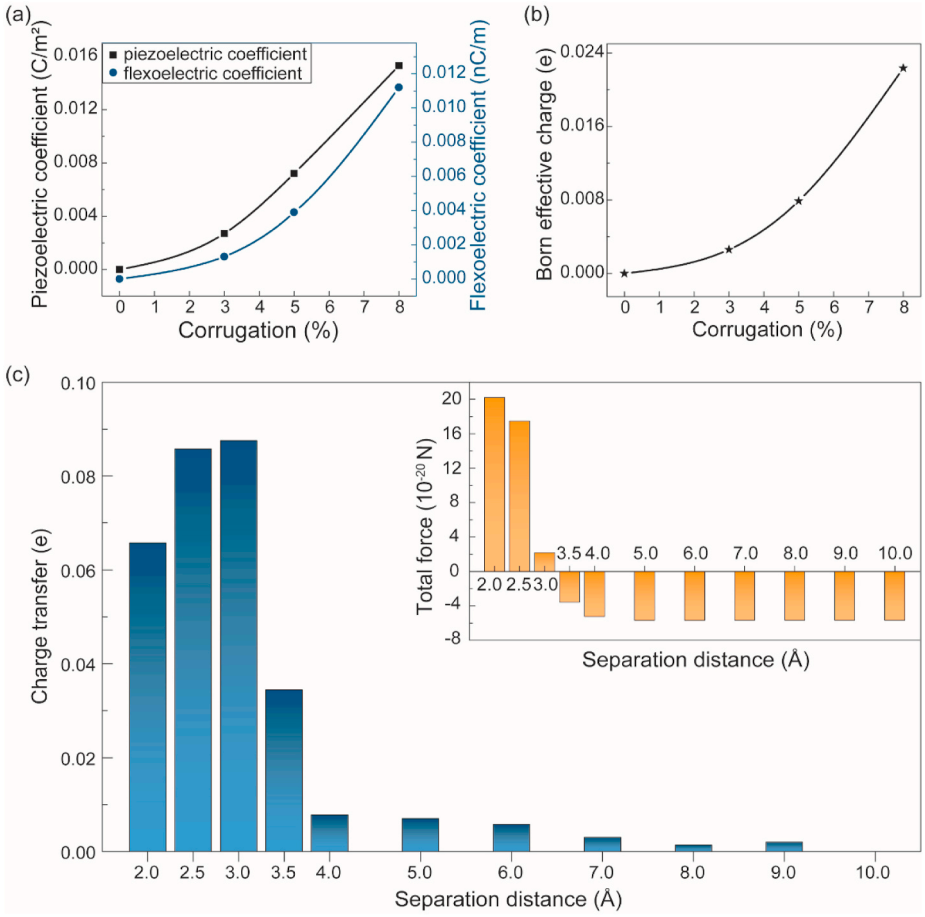

Fig. 7. (a) Induced piezoelectric coefficient e_{zxz} and flexoelectric coefficient μ_{zxzx} of graphene for different corrugations. (b) Corresponding Born effective charge. (c) Charge transfer at different separation distances where the corrugation is 8%. Inset: Corresponding force along the z axis between two layers.

Acknowledgment

This work was supported by the Talent 1000 Program for Foreign Experts, China. Useful discussions with Dr. Yuan Xiang, at the George Washington University, is gratefully acknowledged.

Appendix A. Supplementary data

Supplementary data to this article can be found online at https://doi.org/10.1016/j.nanoen.2020.105386.

References

[1] C. Wu, A.C. Wang, W. Ding, H. Guo, Z.L. Wang, Triboelectric nanogenerator: a foundation of the energy for the new era, Adv. Energy Mater. 9 (2019) 1802906.
[2] Y. Chen, X. Pu, M. Liu, S. Kuang, P. Zhang, Q. Hua, Z. Cong, W. Guo, W. Hu, Z. L. Wang, Shape-adaptive, self-healable triboelectric nanogenerator with enhanced performances by soft solid–solid contact electrification, ACS Nano 13 (2019) 8936–8945.
[3] Z.L. Wang, J. Chen, L. Lin, Progress in triboelectric nanogenerators as a new energy technology and self-powered sensors, Energy Environ. Sci. 8 (2015) 2250–2282.
[4] Z.L. Wang, L. Lin, J. Chen, S. Niu, Y. Zi, Triboelectric Nanogenerators, Springer International Publishing, Switzerland, 2016.
[5] Z.L. Wang, Triboelectric nanogenerators as new energy technology for self-powered systems and as active mechanical and chemical sensors, ACS Nano 7 (2013) 9533–9557.
[6] Z.L. Wang, A.C. Wang, On the origin of contact-electrification, Mater. Today 30 (2019) 34–51.
[7] S. Lin, C. Xu, L. Xu, Z.L. Wang, The overlapped electron-cloud model for electron transfer in contact electrification, Adv. Funct. Mater. 30 (2020) 1909724.
[8] C. Xu, Y. Zi, A.C. Wang, H. Zou, Y. Dai, X. He, P. Wang, Y.-C. Wang, P. Feng, D. Li, Z.L. Wang, On the electron-transfer mechanism in the contact-electrification effect, Adv. Mater. 30 (2018) 1706790.
[9] C. Xu, B. Zhang, A.C. Wang, H. Zou, G. Liu, W. Ding, C. Wu, M. Ma, P. Feng, Z. Lin, Z.L. Wang, Contact-electrification between two identical materials: curvature effect, ACS Nano 13 (2019) 2034–2041.
[10] J. Nie, Z. Ren, L. Xu, S. Lin, F. Zhan, X. Chen, Z.L. Wang, Probing contact-electrification-induced electron and ion transfers at a liquid–solid interface, Adv. Mater. 32 (2020) 1905696.
[11] K.M. Forward, D.J. Lacks, R.M. Sankaran, Charge segregation depends on particle size in triboelectrically charged granular materials, Phys. Rev. Lett. 102 (2009), 028001.
[12] S.R. Waitukaitis, V. Lee, J.M. Pierson, S.L. Forman, H.M. Jaeger, Size-dependent same-material tribocharging in insulating grains, Phys. Rev. Lett. 112 (2014) 218001.
[13] L.L. Ma, W.J. Chen, Y. Zheng, Flexoelectric effect at the nanoscale, in: S. Schmauder, C. Chen, K.K. Chawla, N. Chawla, W. Chen, Y. Kagawa (Eds.), Handb. Mech. Mater., Springer, Singapore, 2018, pp. 1–42.
[14] B. Wang, Y. Gu, S. Zhang, L.-Q. Chen, Flexoelectricity in solids: progress, challenges, and perspectives, Prog. Mater. Sci. 106 (2019) 100570.
[15] X. Zhuang, B. He, B. Javvaji, H.S. Park, Intrinsic bending flexoelectric constants in two-dimensional materials, Phys. Rev. B 99 (2019), 054105.
[16] B. Javvaji, B. He, X. Zhuang, The generation of piezoelectricity and flexoelectricity in graphene by breaking the materials symmetries, Nanotechnology 29 (2018) 225702.
[17] C.A. Mizzi, A.Y.W. Lin, L.D. Marks, Does flexoelectricity drive Triboelectricity ? Phys. Rev. Lett. 123 (2019) 116103.
[18] B.N.J. Persson, On the role of flexoelectricity in triboelectricity for randomly rough surfaces, Europhys. Lett. 129 (2020) 10006.
[19] J. Wu, X. Wang, H. Li, F. Wang, Y. Hu, First-principles investigations on the contact electrification mechanism between metal and amorphous polymers for triboelectric nanogenerators, Nanomater. Energy 63 (2019) 103864.
[20] J. Wu, X. Wang, H. Li, F. Wang, W. Yang, Y. Hu, Insights into the mechanism of metal-polymer contact electrification for triboelectric nanogenerator via first-principles investigations, Nanomater. Energy 48 (2018) 607–616.
[21] L. Li, X. Wang, P. Zhu, H. Li, F. Wang, J. Wu, The electron transfer mechanism between metal and amorphous polymers in humidity environment for triboelectric nanogenerator, Nanomater. Energy 70 (2020) 104476.
[22] C.E. Dreyer, M. Stengel, D. Vanderbilt, Current-density implementation for calculating flexoelectric coefficients, Phys. Rev. B 98 (2018), 075153.

[23] W. Shi, Y. Guo, Z. Zhang, W. Guo, Flexoelectricity in monolayer transition metal dichalcogenides, J. Phys. Chem. Lett. 9 (2018) 6841–6846.
[24] K.N. Duerloo, M.T. Ong, E.J. Reed, Intrinsic piezoelectricity in 2D materials, Environment 3 (2012) 2871–2876.
[25] G. Kresse, J. Hafner, Ab initio molecular dynamics for open-shell transition metals, Phys. Rev. B 48 (1993) 13115–13118.
[26] G. Kresse, J. Furthmüller, Efficient iterative schemes for ab initio total-energy calculations using a plane-wave basis set, Phys. Rev. B 54 (1996) 11169–11186.
[27] P.E. Blöchl, Projector augmented-wave method, Phys. Rev. B 50 (1994) 17953–17979.
[28] G. Kresse, D. Joubert, From ultrasoft pseudopotentials to the projector augmented-wave method, Phys. Rev. B 59 (1999) 1758–1775.
[29] J.P. Perdew, K. Burke, M. Ernzerhof, Generalized gradient approximation made simple, Phys. Rev. Lett. 77 (1996) 3865–3868.
[30] W. Tang, E. Sanville, G. Henkelman, A grid-based Bader analysis algorithm without lattice bias, J. Phys. Condens. Matter 21 (2009), 084204.
[31] S. Baroni, S. de Gironcoli, A. Dal Corso, P. Giannozzi, Phonons and related crystal properties from density-functional perturbation theory, Rev. Mod. Phys. 73 (2001) 515–562.
[32] M. Willatzen, Z.L. Wang, Theory of contact electrification: optical transitions in two-level systems, Nanomater. Energy 52 (2018) 517–523.
[33] G. Fiori, A. Betti, S. Bruzzone, G. Iannaccone, Lateral graphene–hBCN heterostructures as a platform for fully two-dimensional transistors, ACS Nano 6 (2012) 2642–2648.
[34] Y. Guo, J. Robertson, Band engineering in transition metal dichalcogenides: stacked versus lateral heterostructures, Appl. Phys. Lett. 108 (2016) 233104.
[35] O. Bistoni, P. Barone, E. Cappelluti, L. Benfatto, F. Mauri, Giant effective charges and piezoelectricity in gapped graphene, 2D Mater. 6 (2019), 045015.

Dr. Dan Tan received her Ph.D. degree and B.S. degree from Tianjin University. She spent one year at The George Washington University as a visiting doctoral student in 2017. After graduation, she joined the Beijing Institute of Nanoenergy and Nanosystems as an assistant researcher. Her main research interests include piezoelectricity, triboelectricity and computational materials science.

Dr. Morten Willatzen is a Talent 1000 Foreign Expert and Senior Full Professor at the Beijing Institute of Nanoenergy and Nanosystems, Chinese Academy of Sciences. He also holds a Guest Professor position at the Department of Photonics Engineering, Technical University of Denmark and an Honorary Professorship at the Mads Clausen Institute, University of Southern Denmark. He received his MSc degree from Aarhus University and the PhD degree from the Niels Bohr Institute at the University of Copenhagen. Morten Willatzen's research interests include solid state physics, mathematical physics, piezoelectricity, metamaterials and flow acoustics

Dr. Zhong Lin Wang is a Hightower Chair and Regents's Professor at Georgia Tech. He is also the Chief scientist and Director for the Beijing Institute of Nanoenergy and Nanosystems, Chinese Academy of Sciences. His discovery and breakthroughs in developing nanogenerators establish the principle and technological road map for harvesting mechanical energy from environmental and biological systems for powering personal electronics. He coined and pioneered the field of piezotronics and piezo-phototronics by introducing piezoelectric potential gated charge transport process in fabricating new electronic and optoelectronic devices.